Self-similar Mesocrystals Form Via Interface-Driven Nucleation and Assembly

Guomin Zhu[1,2], Maria L. Sushko[1], John S. Loring[1], Ben Legg[1,2], Miao Song[1], Jennifer A. Soltis[1], Xiaopeng Huang[1], Kevin M. Rosso[1], and James J. De Yoreo[1,2,*]

1 Physical Sciences Division, Pacific Northwest National Laboratory, Richland, WA 99354, USA.

2 Department of Materials Science and Engineering, University of Washington, Seattle, WA 98195, USA.

* Correspondence to: Email: james.deyoreo@pnnl.gov.

Crystallization by particle attachment (CPA), which is a common mechanism of colloidal crystallization resulting in hierarchical morphologies[1-4], has been both exploited to create nanomaterials with unique, emergent properties[4-6] and implicated in the development of complex mineral textures[1,7]. Oriented attachment (OA)[7,8], a form of CPA in which crystalline primary particles align and attach along specific crystallographic directions, produces structures — typically referred to as mesocrystals — that diffract like single crystals, even though the constituent particle domains are still discernable[2,9]. While the existence of mesocrystals has been well documented in a wide range of crystal systems[1-9] and individual particle attachment events have been directly visualized[10], the mechanism by which these seemingly random events lead to well-defined, self-similar morphologies remains a mystery, as does the role of organic ligands, which are ubiquitous in nanoparticle systems[3,9,11]. Combining *in situ* TEM at 80°C with "freeze-and-look" TEM using indexed grids, we tracked formation of hematite (Hm) mesocrystals in the presence of oxalate and interpreted the results using classical density functional theory. The results show that formation of isolated Hm particles rarely occurs. However, once formed, interfacial gradients created by hematite-bound oxalate drive new hematite particles to repeatedly nucleate about 2 nm away from the new interface and then immediately undergo OA. Because Hm nucleation rates are

statistically deterministic and direction-specific, the resulting mesocrystals are self-similar. Comparison to natural and synthetic systems suggests interface-driven pathways are widespread.

The conventional view of OA is that nucleation and particle assembly are distinct events. That is, nucleation provides a supply of primary particles, which encounter other primary particles or particle aggregates via Brownian motion biased locally by attractive interparticle potentials. However, many mesocrystals exhibit highly regular morphologies and uniform size distributions, with shapes that appear similar irrespective of size or location, which calls into question how a random nucleation, diffusion and aggregation process can underlie their formation. (Random cluster-cluster aggregation is predicted to produce power-law cluster size distributions[12].)

Attempts to understand how the initial nuclei evolve to a mesocrystal via OA have been complicated by the fact that, in many mineral systems, the first particles to form during crystallization are often of a distinct phase from that of the stable bulk phase[1,13,14]. Consequently, OA often occurs in concert with a phase transformation such that the resulting mesocrystal consists of the bulk phase instead of the primary phase. Little is known about the role of starting primary phase, how or when phase transformation and ordering takes place. While some studies have proposed that particles convert before attachment[15], others have attributed conversion to the attachment process itself[16] and still others have concluded that transformation occurs after the mesocrystal exceeds a characteristic size[14,17]. Still further confounding attempts to develop a predictive understanding of OA is the fact that nanoparticles, whether synthetic or natural, are typically coated with surface-bound ligands[18] and thus studies on bare nanoparticles provide limited insight into the vast majority of OA systems[9]. While all but a few of the above studies based their conclusions on morphological and structural data obtained post-synthesis, they nonetheless highlight the key knowledge gaps in understanding of OA mechanisms and pathways. To address these gaps, we investigated mesocrystal formation of iron oxides, which are amongst the most important colloidal phases in natural environments[19,20]. Iron oxides present classic examples of systems that both form ubiquitous precursor phases and undergo OA accompanied by phase transformations to more stable forms[15,20-22]. Moreover, in soils, where iron oxides are amongst the most common mineral phases, organic constituents, such as oxalate (Ox), are abundant and commonly associate with mineral surfaces, thus the role of organic adsorbates is of particular importance[23].

We started with a precursor consisting of aggregates of poorly crystalline two-line ferrihydrite ($Fe_2O_3{\cdot}xH_2O$, Fh)[20], as verified by the electron diffraction, which exhibited the two characteristic diffuse rings at approximately 1.5 Å and 2.5 Å (Fig. 1a) (see SI for details on preparing Fh). In the absence of additives, single crystals of Hm (Fe_2O_3) with well faceted surfaces formed within 10 hours (Fig. S1a-c). However, upon addition of 2 mM sodium oxalate (NaOx), after two hours, spindle-shaped Hm began to appear within the Fh aggregates (Fig. 1b). By 10 hours, all Fh disappeared, and only spindle-shaped Hm mesocrystals remained. (Fig. 1c and Fig. S1d-f) Cryo TEM at similar time points confirmed these *ex situ* results (Fig. S2). HRTEM shows that all spindles consisted of assemblages of crystallographically aligned primary Hm particles (Fig. 1d-f) and were elongated along the [001] axis (see SI for identifying the elongation). We used an ultramicrotome to make cross sectioned TEM samples of the spindles. The cross sectional TEM (Fig. S3), together with the 3D tomography (Movie M1) confirmed the structure of the spindles and showed that they contained many nm-scale pores.

Dimensional analysis of the spindles showed that the size of the primary particles increased from about 3.5 nm at 2 hours, (Fig. 1d) to 6.5 nm at 10 hours (Fig. 1e) to 9.5 nm at 200 hours (Fig. 1f). A plot of spindle length vs. width revealed a constant aspect ratio of about 2.15 ± 0.08 for all

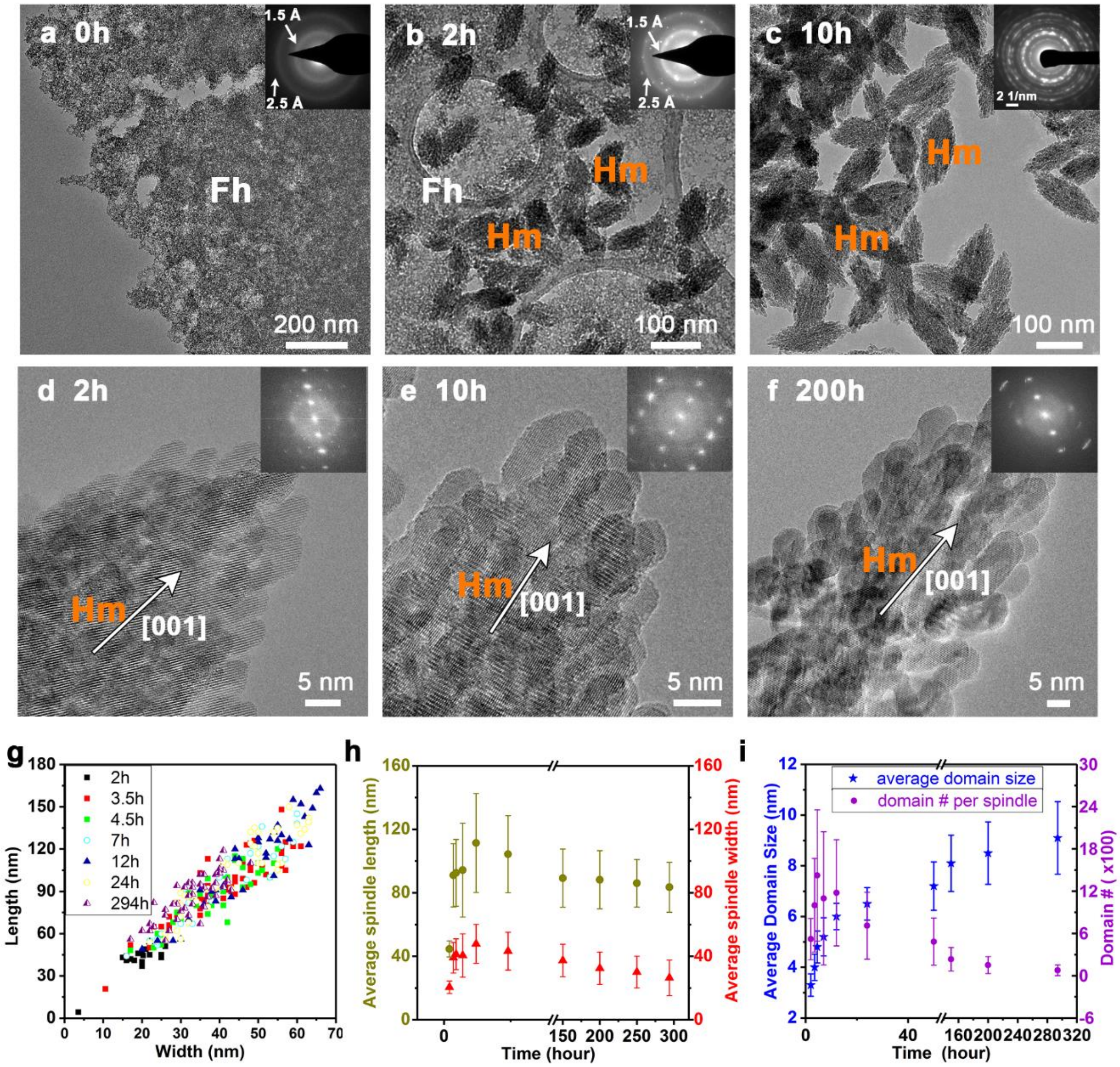

Fig. 1 **Formation of spindle-shaped Hm mesocrystals from Fh nanoparticles**. **a** Ex situ TEM image of Fh aggregate, with selected area electron diffraction (SAED) showing two diffuse rings. **b** Spindle-shaped Hm appeared in 2 hours. **c** Transformation of all the Fh to Hm occurred by 10 hours. **d-f** HRTEM images of spindle-shaped Hm exhibiting crystallographically coaligned domains whose sizes increase with time. Insets: FFTs performed on whole images. **g** Spindle length vs. width, showing constant aspect ratio. **h** Plots of average spindle length (green color) and width (red color) as a function of time. **i** Plots of average domain size (blue color) and domain number per spindle (purple color) as a function of time. (After about 10 hours, the product of average domain volume and number is approximately constant.)

spindles and all times in multiple experiments, demonstrating the deterministic nature of spindle growth. Because the primary particles are approximately spherical and uniformly distributed, this constant aspect ratio implies the particle addition rate was ~ 2.2 times faster along the [001] than along the [hk0] directions. Moreover, this consistency was maintained even though the average spindle length and width both increased for the first 12 hours and decreased thereafter (Fig. 1g and h, Table S1). In contrast to the aspect ratio, the sizes of the spindles varied greatly at any given time. For example, at 3.5 hours, spindle length and width varied from 10 nm to 60 nm and 20 nm to 140 nm, respectively. This factor of 6 to 7 spread in sizes reflects the slow but continuous birth of new spindles as long as Fh is present in the solution.

The analysis also shows that spindle development proceeded in two stages: During the first stage, spindles grew in length, width and particle number. During the second stage, spindle size decreased, but the average primary particle size continued to grow while the total number of discernable particles decreased so that the total volume particles in a spindle remained nearly constant (Fig. 1i), while the exposed particles slowly grew (Fig. 1i) and developed facets (Fig. 1e and 1f). The transition from the first to second stage correlated with disappearance of the Fh (Fig. 1c and i). These results imply that the first stage is dominated by spindle growth through continual addition of Hm particles that form at a solution saturation state set by the more soluble Fh, which gradually decreases in mass. In contrast, the second stage is dominated by particle coarsening in a solution at equilibrium with respect to Hm and devoid of Fh.

To track the evolution of Fh and Hm over time, we used a "freeze and look" method by loading indexed TEM grids with Fh and imaged the grids over time. The Fh-loaded grids were then placed into Ox-containing solution at 90 °C (see SI for details). The grids were returned to the TEM for imaging in the same regions after a few hours of reaction (Fig. 2a and Fig. S4). Fh on the indexed

TEM grid was observed to consist initially of large aggregates (Fig. 2b). After 3 hours, the overall morphology of the Fh aggregates was preserved and the first Hm particles began to appear, but were only found amongst the Fh aggregates (Fig. 2c). Given that the solution must be in equilibrium with Fh, the fact that Hm only exists in association with the Fh implies that the initial Hm particles must form either through transformation of Fh or heterogeneous nucleation at the Fh/solution interface.

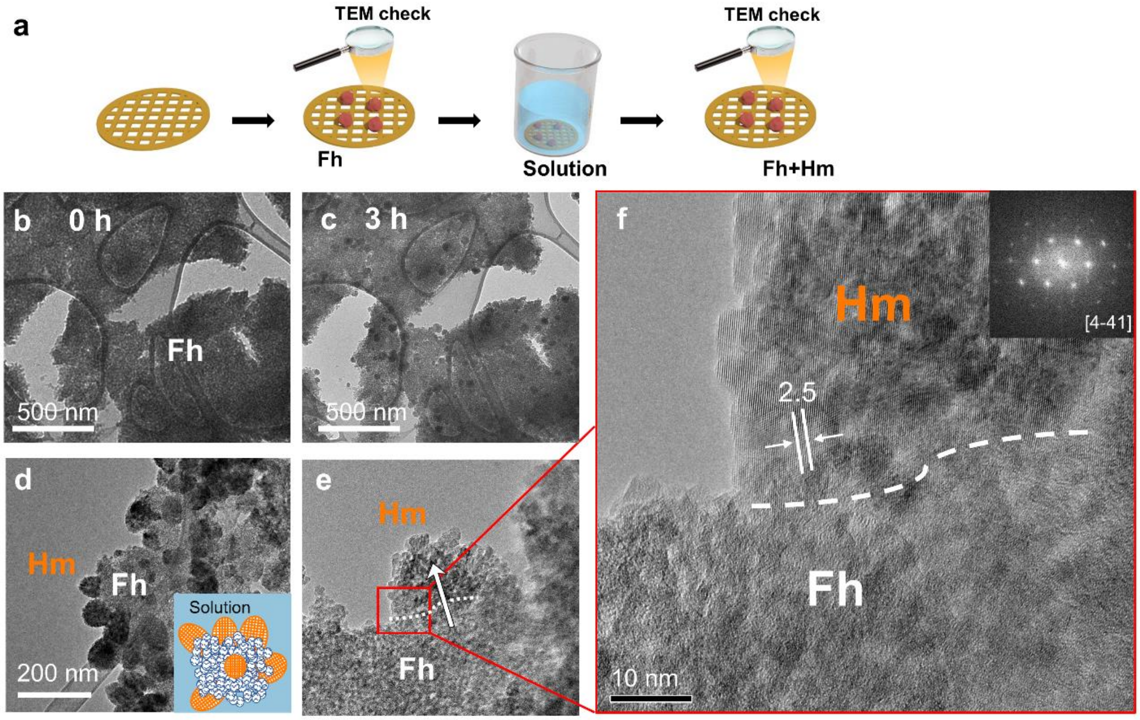

Fig. 2 **Relationship between developing Hm spindles and Fh precursor**. **a** Schematic of experimental approach using indexed TEM grids to follow the reaction at a given location over time. **b** Aggregates of Fh deposited on an indexed lacy carbon TEM grid. **c** Appearance of Hm particles among the Fh aggregates after 3 hours. **d** Representative images of Hm particles and half-spindles on the edge of the Fh aggregates. Inset illustrates the aggregates of Fh (blue) with half spindles (red) growing on the top and pointing towards the solution. **e, f** TEM images of a half-spindle Hm pointing away from the Fh and into the solution, with crystallographically coaligned domains. The Fh-Hm boundary is marked by the dashed line. The half spindle is elongated along the [001] axis denoted by the white arrow.

A closer examination of the Hm particles showed that they exhibited a half-spindle shape with all of the Hm half-spindles pointing towards solution rather than into the Fh aggregate (Fig. 2d). HRTEM near the spindle-Fh interface (Fig. 2e and f) shows the primary Hm particles are crystallographically coaligned (see inset FFT pattern) and spindles formed in this manner are also elongated along the c axis. If the Hm spindles were growing through direct addition of Fh, which then transformed to Hm, we would expect the spindle to be growing into the aggregate of Fh particles, i.e., the tip of the spindle would advance toward the source of the Fh particles. The fact that the spindle tip advances towards the Fh source and into the bulk solution implies that the Hm primary particles are instead forming and adding from the surrounding solution. (This process did not occur on the Fh side of the spindle, which was a fixed, dense mass of Fh nanoparticles, showing that direct Fh transformation to Hm is not the source of the Hm primary particles in the spindles)."

If the Hm particles come from the solution surrounding the forming spindles, the implication of a time-independent spindle shape and aspect ratio is that the first formed Hm particles determine the rate of production and attachment of subsequent particles. To further explore this possibility, well faceted single crystal seeds of Hm, which have exposed (001) and (012) facets, were added to sodium Ox containing solutions of Fh precursor particles. The number density of seeds was negligible compared to the Fh, mimicking the situation early in stage 1. The results show that Hm spindles indeed grew around these Hm seeds. After incubating for 5 hours, Hm primary particles had formed and attached to the Hm seeds in crystallographic coalignment with the seeds to create spindles for which the ratio of the added length to the added width was again 2.2. (Fig. 3a; see SI for details, and Fig. S5 for more examples) Thus seeded Hm growth follows the same crystallization pathway as unseeded growth, with the seed providing a template for the organization of the new Hm particles. When the reverse experiment was run and Hm spindles were added to Fh containing solutions free of Ox, Hm with well faceted surfaces grew over the Hm spindles. Moreover, the well faceted Hm was crystallographically coaligned with the encapsulated Hm spindle. (Fig. S6).

The above observations suggest that, once Hm particles are present in solutions of Fh and sodium Ox — whether through nucleation of Hm from solution, on the Fh, or by seeding — the Fh then serves only as a source of solute and all subsequent Hm particles form from the solution that surrounds existing Hm crystals. These new particles must nucleate either directly on the initial Hm crystals in crystallographic coalignment or in the solution near the Hm crystals and then attach in a coaligned fashion. To test this hypothesis and determine where the new Hm particles formed, we exploited the ability to grow spindles on existing Hm seeds by using *in situ* liquid phase TEM with a heating holder operating at 80°C[24-26].

In TEM mode, initially, the Hm seeds were clearly resolved, but the Fh particles were difficult to see due to their low contrast (Fig. 3c and Movie M2). However, STEM imaging simultaneously resolved both the Hm seeds and the Fh particles (Fig. S7 and movie M3). The combined results show that the Fh gradually dissolves, while new Hm particles nucleate adjacent to — but not on — the surface of the Hm seeds and then attach to the seeds (arrows in Fig. 3c-e). Moreover, the spheroidal shape of the nuclei and large contact angles of over 90° between seed and nucleus are inconsistent with heterogeneous nucleation on the seed surface, where nucleation would only be preferred if the interfacial energy, and hence the contact angle, was low. In addition, the flat faces of the seed away from the locations of the attached particles do not grow significantly and do not develop roughness at the scale of a nm or more. This is consistent with the observation that, during late-stage coarsening, the exposed particle surfaces develop facets (Figs. 1e and 1f). When the experiment was allowed to progress for extended periods of time during which the beam was blocked between collection of multiple short image series (Fig. 3e and Movie M6 and M7), the development of spindles around the seeds and the repeated nucleation and attachment of new

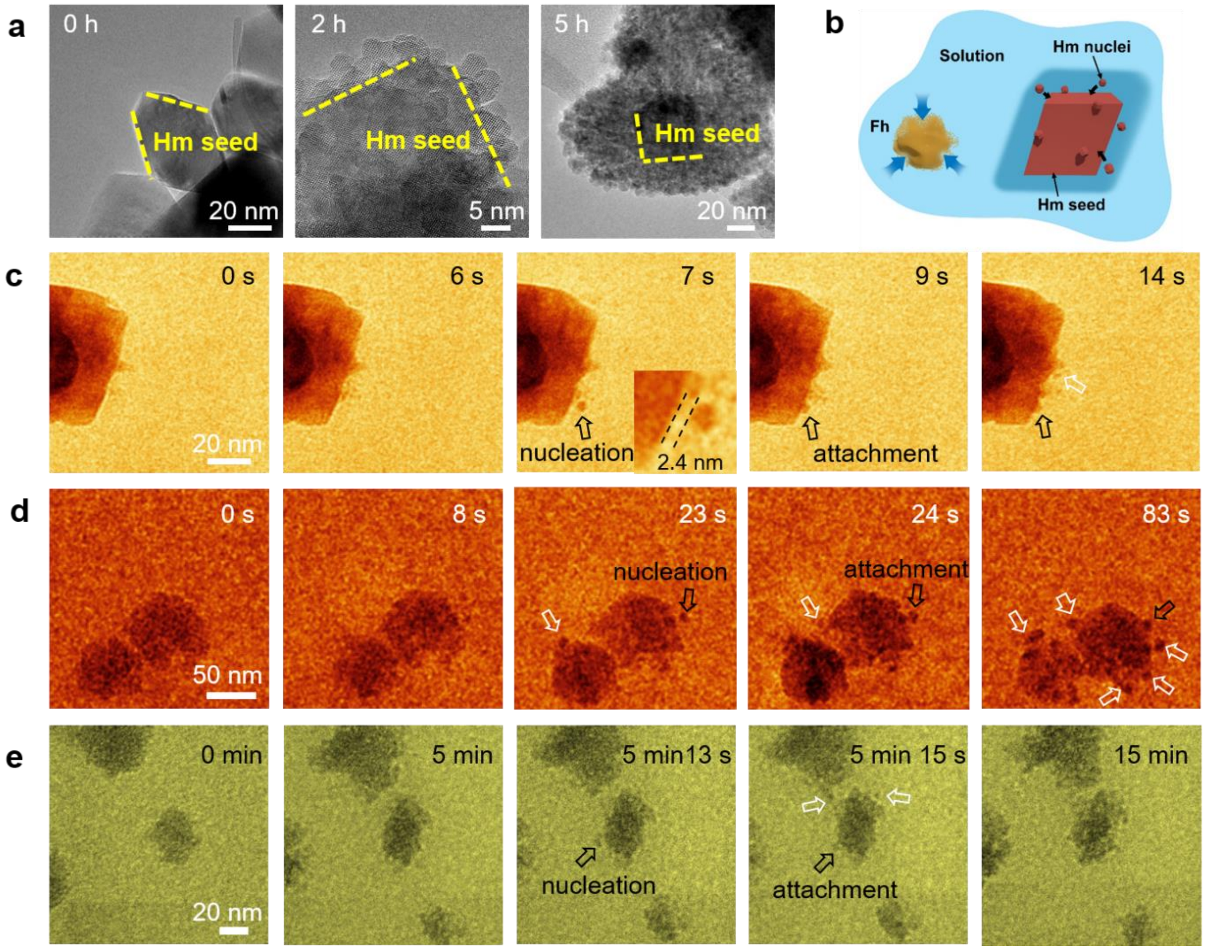

Fig. 3 Liquid phase TEM observation of Hm nucleation close to the Hm-solution interface and subsequent attachment to form Hm spindles. a Hm seeds with initital smooth surfaces are covered with primary particles after 2 hours and develop into fully-formed spindles by 5 hours, as confirmed by *ex situ* TEM. **b** Cartoon showing the dissolution of Fh, and near-interface Hm nucleation and attachment to Hm seeds. **c** and **d** Sequential in situ TEM images from movie M5 and M2 collected at 80°C showing Hm nucleation close to Hm-solution interface followed by attachment to the seed. The black arrows highlight particles that nucleate and then attach to the seed. For the series in **c**, a surface-to-surface gap of 2.4 nm is measured at 7s (inset), the spheroidal particle is attached to the seed with a contact angle over 90° at 9s and coarsens to eliminate the negative curvature created by the attachment event by 14s. Additional nucleation events are indicated by the white arrows. **e** Sequential TEM images from movie M6 showing the growth of multiple Hm spindles from Hm seeds, like those in **b** and **c**, over a time period of about 15 minutes. The electron beam was blocked for most of time course of the experiment, with beam exposure only occurring for collection of short image series in the middle of the experiment. The black arrows highlight near-interface nucleation at about 5min 13s, and attachment to the mother particle near 5min 15s, featured by the black arrow. Additional near-interface nucleation events are highlighted by the white arrows.

particles to the growing spindles could be directly followed. Analysis of the liquid cell contents after *in situ* heating for 8 hours showed that the final products were indistinguishable from the spindles formed *ex situ* (Fig. S8 vs. Fig. 1c), thus confirming the fidelity of heated liquid phase TEM experiments to the experiments done in bulk solution, as well as those using indexed TEM grids.

The *in situ* TEM results provide clear evidence that Fh acts as a buffer to provide the source and set the concentration of solute ions from which new Hm primary particles form. As long as Fh particles are present, the solute concentration remains fixed at the solubility of Fh ensuring that the Hm particles form at constant supersaturation as the Fh dissolves to replace the ions taken up by the growing Hm. However, these new Hm particles nucleate near the Hm-solution interface, exhibiting an intervening edge-to-edge gap of about 1-3 nm before attaching to build the spindle-shaped Hm monocrystals, though the 2D nature of TEM imaging and resolution limits preclude a precise determination of the initial separation (see SI for a detailed analysis, Fig. S9). The fact that all new Hm particles attach to the parent seed or spindle and none are found diffusing into the bulk solution far from the seed (or spindle), is a clear reflection of motion within a potential that attracts the dauighter particles to the parent seed or spindle around which they nucleate. However, we cannot discern from these experiments whether the new Hm particles are coaligned upon nucleation, align during attachment, or whether they exhibit other styles of OA[1] including attachment with some misalignment followed by elimination of defects,[10,27] or, perhaps in some instances, attachment via formation of neck in the intervening gap.[28,29]

What is the role of Ox then? In solution, Ox binds with Fe^{3+} to make Ox complexes the dominant Fe-species down to pH values well below those used here [30]. Ox is therefore capable of accelerating Fh dissolution, though it does not appreciably shift the bulk Fe^{3+} activity, which still remains fixed at the solubility of Fh. However, the difference in Hm growth with and without Ox shows it also acts at the Hm surface: In the absence of Ox, Hm forms large faceted crystals (Fig. 3a and S1a), while in its presence approximately spheroidal particles are formed, which presumably grow ion-by-ion but only grow very slowly once they reach about ~ 5nm in diameter. Consequently, one role of Ox is to stabilize Hm nanoparticles and inhibit their growth. Moreover, in the absence of Ox, we find no evidence for aggregation of Hm particles, suggesting that Ox resides at the Hm particle surface and biases the local chemistry to promote Hm nucleation and possibly assist in OA.

To test the above hypothesis, we first measured the degree to which Ox binds to the common (001) and (012) faces of Hm using attenuated total reflection Fourier transform infrared (ATR-FTIR) spectroscopy and ion chromatography[31]. The results show that the Hm (001) and (012) surfaces develop high Ox coverages of 4.38 and 12.17 Ox molecules per nm^2, (respectively Fig. 4a, and Table S2). Calculations using plane wave density functional theory (see SI for details) gave similar results of 4.30 and 13.92 Ox anions per nm^2 at full coverage with Ox exhibiting strong bidentate end-on mononuclear binding on both Hm faces (Fig. S11 and Table S2) consistent with prior analyses[32,33].

We then performed classical density functional theory (cDFT) calculations, which are ideal for modeling the chemical potential of ions within complex multicomponent electrical double layers, to determine the impact of Ox on the Fe^{3+} concentrations near the interface, as well as the corresponding Hm-Hm interparticle forces (Fig. 4b). Following an approach that separates contributions to the total chemical potential describing entropy of mixing (ideal chemical potential) and all interfacial interactions (potential of mean force) (See SI for details), our cDFT analyses show that the driving forces for Fe^{3+} accumulation at the surface of a Hm particle exhibit a qualitative difference in Fe^{3+} potential of mean force with and without Ox in solution. Without Ox, potential of mean force is dominated by the short-range Fe/surface interactions and the shape

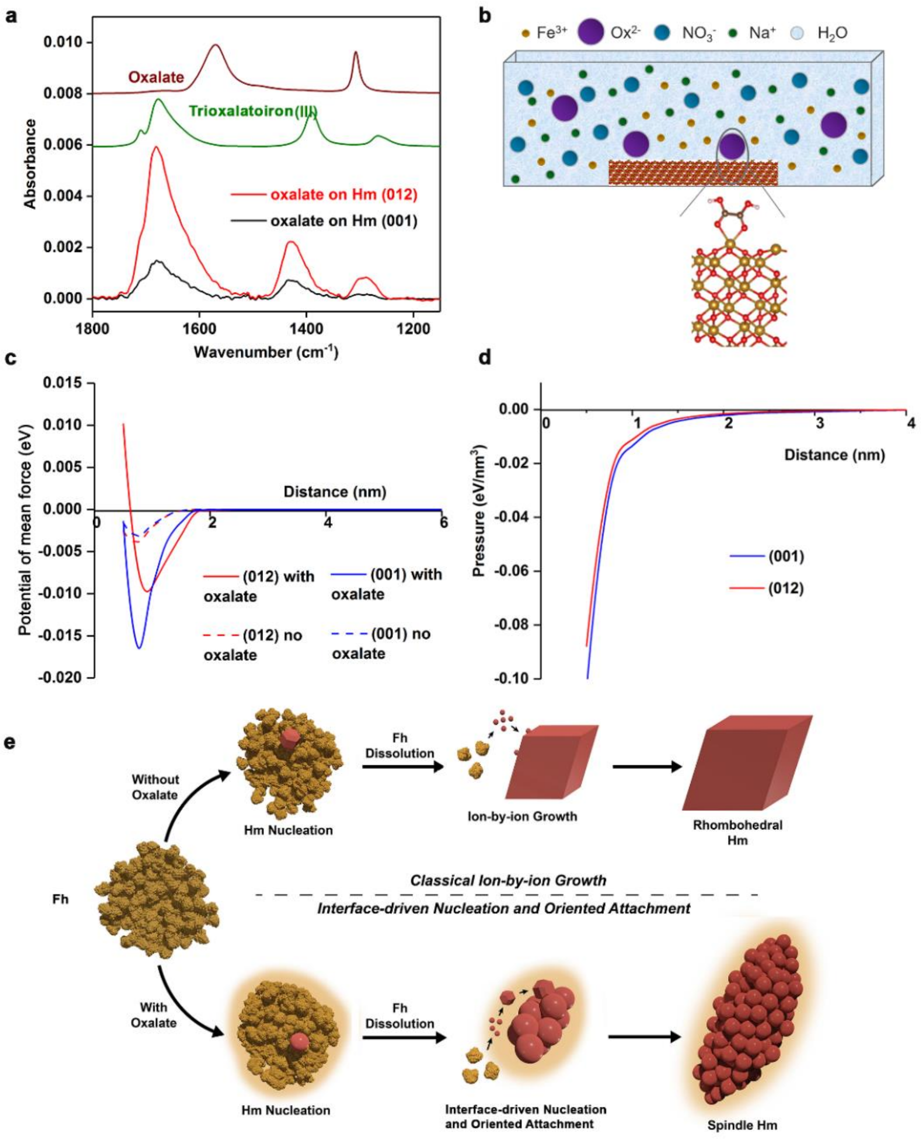

Fig. 4 **Structure and thermodynamics of Hm-solution interface. a** ATR-IR spectra of Ox adsorbed on Hm (001) vs. Hm (012). The offset spectra of trioxalatoiron (III) and the aqueous Ox anion are models for inner-sphere bidentate-mononuclear and outer-sphere water-separated binding, respectively (24). Comparison of the spectra of adsorbed Ox to these reference spectra indicates that Ox is predominantly bound to Hm through direct surface Fe (III) coordination in a bidentate mononuclear fashion. **b** Schematic of the solution speciation and simulation set-up. **c** Average potential of mean force of Fe ions vs. distance away from the surface with and without Ox. **d** Distance dependence of particle-particle interaction showing barrier free attraction, which biases the aggregation. **e** Schematic of ion-by-ion growth vs. interface driven nucleation and oriented attachment, without oxalate and with oxalate, respectively. In the latter case, the process is as follows: Hm first nucleates within the Fh aggregate leading to depletion of solute ions in the solution. Thus Fh begins to dissolve to maintain the equilibrium solution speciation. The oxalate/Hm/solution interface then drives nucleation of new Hm particles near interface and the newly formed particles, which initially grow ion-by-ion to about 5 nm, undergo OA to attach to the growing spindle, while. Fh continues to dissolve to maintain equilibrium. After all the Fh is consumed, the Hm particles in the spindle continues to coarsen through slow ion-by-ion growth.

of its distance dependence predicts a barrier-free process of ion addition. In contrast, in the presence of Ox surface complexes, which create a layer of negatively charged discrete sites, the potential of mean force of Fe^{3+} is dominated by the entropic ion correlation interactions, which stabilize the interfacial diffuse layer of solvated Fe^{3+} hindering diffusion and deposition on the surface. Solvation interactions contribute to the chemical potential barrier (Fig. S11c). These two factors lead to Fe^{3+} accumulation approximately 1 nm away from the surface, which is approximately the same region in which nucleation of new Hm particles is observed (Fig. 4c). While the chemical potential of Fe^{3+} relative to bulk hematite must be constant throughout a well-mixed system, these results predict that the solution chemistry in the interfacial region differs from that of the bulk and the greatest difference occurs about 1 nm from the surface.

Nucleation rates in the interfacial region may be enhanced for both kinetic and thermodynamic reasons. Kinetic effects should only scale linearly with the concentration of precursor species. For Fe^{3+}, the concentration enhancements predicted by cDFT would have a negligible effect on the kinetic pre-factor, although some other Fe-oxalate complexes may be more significantly influenced (See SI for details). Thermodynamic barriers, however, may be dramatically affected. For homogenous nucleation of spherical nuclei, the energy of forming a critical nucleus is typically estimated as $\Delta G^{crit} = -\frac{16}{3}\pi\omega^2\alpha^3/kT\Delta\mu^2$ where ω is the volume per growth molecule in the solid, α is the interfacial free energy, and $\Delta\mu$ is difference in chemical potential between the solution and the bulk solid. The absence of nucleation in the bulk solution indicates that this barrier is very high; indeed we estimate the value to be on ~ 80kT (see SI). However, models of heterogeneous nucleation[34], have shown that such barriers can be dramatically reduced if clusters have favorable interactions with interfaces due to reductions in α. Such treatments are probably oversimplified, since clusters interact with surfaces in diverse ways that may cause the form of the energy landscape to deviate from classical scaling laws. A reduction of the effective interfacial free energy of just 5% would enhance nucleation rates by a factor of $e^{19.6} = 3.3E8$ (see SI for details).

Other evidence suggests that solubilities are altered in confined spaces, thin solution layers and near organic interfaces, resulting in necking between nanoparticles and the deposition of crystalline films[35,36]. A reduced hematite solubility would lead to an increased value of $\Delta\mu$ near the interface; a reduction by just 10% would increase the predicted rate by $e^{10} = 2.2E4$.

Remarkably, the TEM evidence suggests that nucleation is most favored roughly a couple of nanometers from the hematite surface, rather than directly on the surface, indicating that the barrier to nucleation is smallest in this region. This is consistent with the predictions of the cDFT simulations that Fe^{3+} species are most concentrated roughly 1 nm from the oxalate-covered Hm surfaces. Moreover, because the oxalate coverage differs on distinct crystallographic faces (Figure 4a,c) — as should the structure of the hydration layers[37] — we can expect direction dependent nucleation rates, which will generate anisotropic mesocrystal morphologies, such as the spindle-shape crystals obtained here. Following nucleation and growth of the new Hm particles, the cDFT calculations of corresponding interparticle forces predict that they should attach to the primary particles along a barrier-free attractive inter-particle potential, which is mainly due to van der Waals interactions, with weak facet specificity of the attractive inter-particle pressure arising from ion correlation interactions (Fid. 4d and S11e and f).

The collective findings reported here converge on an important new pathway of CPA that resolves some key questions about mesocrystal formation (Fig. 4e). Ligands associated with nanocrystal surfaces can bias nucleation to occur in the interfacial region near the surface where attractive interactions then drive attachment. Thus, the processes of nucleation and particle aggregation that have been traditionally viewed as separate are instead inherently linked and bias the growth pathway away from conventional ion-by-ion growth towards OA. Moreover, one of the key characteristics of Hm spindle-shaped particles, namely the self-similar morphology of branched nanoparticle aggregates with uniform aspect ratio, can now be understood as arising naturally from this interface-driven process of nucleation and OA. Given that the system investigated here presents typical characteristics of nanoparticle systems — i.e., the particles form from an initial metastable phase, they are stabilized by organic ligands, and they exhibit attractive interactions at short range — this proposed pathway may be able to account for numerous occurrences of mesocrystal formation, which include, for example, $BaCO_3$, $BaSO_4$, TiO_2, CuO, and ZnO, etc.[2,9,38], many of which also occur in spindle-shaped morphologies (Fig. S12)[9,39,40]. Moreover, these results point towards a strategy for synthesizing mesocrystalline materials with control over size, shape and uniformity. The phenomenon observed here suggests mixtures of ligands that exhibit face-specificity of binding can be used to drive nucleation of new particles adjacent to the surfaces of seed crystals with similar face-specificity. Thus, with the proper choice of bulk supersaturation, ligand coverage, and ligand chemistry, one could presumably control the direction-specific rate of particle generation and attachment.

Evidence for interfacially driven nucleation due to local chemical gradients has been reported for other systems. An investigation of Au nanoparticle growth concluded that when these pH sensitive chemical gradients become comparable, near-surface nucleation followed by particle attachment becomes the dominant growth pathway[28]. The effect of organic films at mineral interfaces on concentrating cations was also invoked to explain the formation of barite in the oceans, which are globally undersaturated with respect to the mineral[35]. Nucleation and growth of barite nanoparticles was shown to occur in slightly undersaturated solutions on COOH- and SHterminated films due to concentration of Sr^{2+} at the charged organic interface. A number of other studies have attributed heterogeneous nucleation due to chemical transformations of precursors near the interface, including reduction of Au and Pd during seeded nanoparticle synthesis [41] and Ni films during electrodeposition from NiCl solutions[42].

Our results also provide a possible explanation for unusual morphologies of naturally occurring iron oxides. The most obvious examples are the strikingly similar spindle-shaped mesocrystalline Hm recently discovered in the classic Precambrian banded iron formations of Australia[43] (Fig. S12), as well as the so called, “rainbow Hm”, whose name reflects the natural iridescence of the mineral, is composed of spindle-shaped Hm 200-300 nm in length and 50-60nm in width[44]. Other studies on iron oxide-rich tropical soils reported Hm and goethite consisting of nanoparticle aggregates, including spindles of similar dimensions[45]. In our study, spindle-shaped Hm formed at temperatures as low as 40°C, suggesting that the process observed here is feasible in these natural settings, where organic constituents, including oxalate, are abundant.

Understanding the mechanisms and dynamics of CPA in natural systems is critical to developing quantitative models for biogeochemical cycling of nutrients and metals, environmental remediation, climate reconstruction based on isotopic and impurity signatures, and the enigmatic textures and compositions of many mineral deposits[1,7,43,46]. Learning to deterministically manipulate CPA will enable advances in nanomaterials design and synthesis for applications in thermoelectrics, photonics, catalysis, and photovoltaics[2-6,47]. Taken together, the findings reported here and the comparisons to other systems suggest that an interface-driven process of CPA may be a widespread phenomenon in both synthetic and natural environments.

ACKNOWLEDGMENTS

This material is based upon work supported by the US Department of Energy (DOE), Office of Science, Office of Basic Energy Sciences, Chemical Sciences, Geosciences, and Biosciences Division, Geosciences Program at Pacific Northwest National Laboratory (PNNL). High resolution TEM and STEM imaging and DFT simulations were performed in the Environmental and Molecular Sciences Laboratory, a DOE Office of Science User Facility at PNNL sponsored by the Office of Biological and Environmental Research. PNNL is a multiprogram national laboratory operated for DOE by Battelle under Contract No. DE-AC05–76RL01830.

Data availability

The data supporting the findings of this study are available from the corresponding authors upon request.

Code availability

The codes used for the findings of this study are available from the corresponding author upon request.

REFERENCES

1 De Yoreo, J. J. *et al.* CRYSTAL GROWTH. Crystallization by particle attachment in synthetic, biogenic, and geologic environments. *Science* **349**, aaa6760, doi:10.1126/science.aaa6760 (2015).

2 Sturm , E. V. & Cölfen, H. Mesocrystals: Past, Presence, Future. *Crystals* **7**, 207 (2017).

3 Cho, K. S., Talapin, D. V., Gaschler, W. & Murray, C. B. Designing PbSe nanowires and nanorings through oriented attachment of nanoparticles. *J. Am. Chem. Soc.* **127**, 7140-7147, doi:10.1021/ja050107s (2005).

4 Yang, J. *et al.* Formation of two-dimensional transition metal oxide nanosheets with nanoparticles as intermediates. *Nat. Mater.* **18**, 970-976, doi:10.1038/s41563-019-0415-3 (2019).

5 Whitham, K. *et al.* Charge transport and localization in atomically coherent quantum dot solids. *Nat. Mater.* **15**, 557-563, doi:10.1038/nmat4576 (2016).

6 Boneschanscher, M. P. *et al.* Long-range orientation and atomic attachment of nanocrystals in 2D honeycomb superlattices. *Science* **344**, 1377-1380, doi:10.1126/science.1252642 (2014).

7 Banfield, J. F., Welch, S. A., Zhang, H., Ebert, T. T. & Penn, R. L. Aggregation-based crystal growth and microstructure development in natural iron oxyhydroxide biomineralization products. *Science* **289**, 751-754, doi:10.1126/science.289.5480.751 (2000).

8 Penn, R. L. & Banfield, J. F. Imperfect oriented attachment: dislocation generation in defect-free nanocrystals. *Science* **281**, 969-971, doi:10.1126/science.281.5379.969 (1998).

9 Cölfen , H. & Antonietti, M. Mesocrystals and nonclassical crystallization. doi:10.1002/9780470994603 (2008).

10 Li, D. *et al.* Direction-specific interactions control crystal growth by oriented attachment. *Science* **336**, 1014-1018, doi:10.1126/science.1219643 (2012).

11 Yin, Y. & Alivisatos, A. P. Colloidal nanocrystal synthesis and the organic-inorganic interface. *Nature* **437**, 664-670, doi:10.1038/nature04165 (2005).

12 Sposito, G. Scaling invariance of the von Smoluchowski rate law. *Colloids Surf. A* **120**, 101-110, doi:10.1016/S0927-7757(96)03718-1 (1997).

13 Nielsen, M. H., Aloni, S. & De Yoreo, J. J. In situ TEM imaging of CaCO(3) nucleation reveals coexistence of direct and indirect pathways. *Science* **345**, 1158-1162, doi:10.1126/science.1254051 (2014).

14 Van Driessche, A. E. *et al.* The role and implications of bassanite as a stable precursor phase to gypsum precipitation. *Science* **336**, 69-72, doi:10.1126/science.1215648 (2012).

15 Yuwono, V. M., Burrows, N. D., Soltis, J. A. & Penn, R. L. Oriented aggregation: formation and transformation of mesocrystal intermediates revealed. *J. Am. Chem. Soc.* **132**, 2163-2165, doi:10.1021/ja909769a (2010).

16 Baumgartner, J. *et al.* Nucleation and growth of magnetite from solution. *Nat. Mater.* **12**, 310-314, doi:10.1038/nmat3558 (2013).

17 Navrotsky, A., Mazeina, L. & Majzlan, J. Size-driven structural and thermodynamic complexity in iron oxides. *Science* **319**, 1635-1638, doi:10.1126/science.1148614 (2008).

18 Boles, M. A., Engel, M. & Talapin, D. V. Self-Assembly of Colloidal Nanocrystals: From Intricate Structures to Functional Materials. *Chem. Rev.* **116**, 11220-11289, doi:10.1021/acs.chemrev.6b00196 (2016).

19 Cornell, R. M. & Schwertmann, U. The iron oxides: structure, properties, reactions, occurences and uses, second edition. doi:10.1002/3527602097 (2003).

20 Fischer, W. R. The Formation of Hematite from Amorphous Iron(III)Hydroxide. *Clays and Clay Miner.* **23**, 33-37, doi:10.1346/ccmn.1975.0230105 (1975).

21 Frandsen, C. *et al.* Aggregation-induced growth and transformation of β-FeOOH nanorods to micron-sized α-Fe2O3spindles. *CrystEngComm* **16**, 1451-1458, doi:10.1039/c3ce40983j (2014).

22 Sugimoto, T., Itoh, H. & Mochida, T. Shape Control of Monodisperse Hematite Particles by Organic Additives in the Gel-Sol System. *J. Colloid Interface Sci.* **205**, 42-52, doi:10.1006/jcis.1998.5588 (1998).

23 Graustein, W. C., Cromack, K., Jr. & Sollins, P. Calcium oxalate: occurrence in soils and effect on nutrient and geochemical cycles. *Science* **198**, 1252-1254, doi:10.1126/science.198.4323.1252 (1977).

24 Tan, S. F. *et al.* In Situ Kinetic and Thermodynamic Growth Control of Au-Pd Core-Shell Nanoparticles. *J Am Chem Soc* **140**, 11680-11685, doi:10.1021/jacs.8b05217 (2018).

25 Smith, B. J. *et al.* Colloidal Covalent Organic Frameworks. *ACS Cent. Sci.* **3**, 58-65, doi:10.1021/acscentsci.6b00331 (2017).

26 Xin, H. L. & Zheng, H. In situ observation of oscillatory growth of bismuth nanoparticles. *Nano Lett.* **12**, 1470-1474, doi:10.1021/nl2041854 (2012).

27 Nielsen, M. H. *et al.* Investigating Processes of Nanocrystal Formation and Transformation via Liquid Cell TEM. *Microsc. Microanal.* **20**, 425-436, doi:10.1017/S1431927614000294 (2014).

28 Cheng, Y. *et al.* Near surface nucleation and particle mediated growth of colloidal Au nanocrystals. *Nanoscale* **10**, 11907-11912, doi:10.1039/c8nr03408g (2018).

29 Liu, L. *et al.* Connecting energetics to dynamics in particle growth by oriented attachment using real-time observations. *Nat. Commun.* **11**, 1045, doi:10.1038/s41467-020-14719-w (2020).

30 Lee, S. O., Tran, T., Jung, B. H., Kim, S. J. & Kim, M. J. Dissolution of iron oxide using oxalic acid. *Hydrometallurgy* **87**, 91-99, doi:10.1016/j.hydromet.2007.02.005 (2007).

31 Loring, J. S., Simanova, A. A. & Persson, P. Highly mobile iron pool from a dissolution-readsorption process. *Langmuir* **24**, 7054-7057, doi:10.1021/la800785u (2008).

32 Zhang, Y., Kallay, N. & Matijevic, E. Interaction of metal hydrous oxides with chelating agents. 7. Hematite-oxalic acid and -citric acid systems. *Langmuir* **1**, 201-206, doi:10.1021/la00062a004 (1985).

33 Situm, A., Rahman, M. A., Allen, N., Kabengi, N. & Al-Abadleh, H. A. ATR-FTIR and Flow Microcalorimetry Studies on the Initial Binding Kinetics of Arsenicals at the Organic–Hematite Interface. *J. Phys. Chem. A* **121**, 5569-5579, doi:10.1021/acs.jpca.7b03426 (2017).

34 Hu, Q. *et al.* The thermodynamics of calcite nucleation at organic interfaces: Classical vs. non-classical pathways. *Faraday Discuss.* **159**, 509, doi:10.1039/c2fd20124k (2012).

35 Deng, N. *et al.* Organic-mineral interfacial chemistry drives heterogeneous nucleation of Sr-rich (Ba x , Sr1-x)SO4 from undersaturated solution. *Proc. Natl. Acad. Sci. U. S. A.* **116**, 13221-13226, doi:10.1073/pnas.1821065116 (2019).

36 Jin, B., Sushko, M. L., Liu, Z., Jin, C. & Tang, R. In Situ Liquid Cell TEM Reveals Bridge-Induced Contact and Fusion of Au Nanocrystals in Aqueous Solution. *Nano Lett.* **18**, 6551-6556, doi:10.1021/acs.nanolett.8b03139 (2018).

37 Songen, H. *et al.* Resolving Point Defects in the Hydration Structure of Calcite (10.4) with Three-Dimensional Atomic Force Microscopy. *Phys. Rev. Lett.* **120**, 116101, doi:10.1103/PhysRevLett.120.116101 (2018).

38 Liu, Z. *et al.* Intrinsic dipole-field-driven mesoscale crystallization of core-shell ZnO mesocrystal microspheres. *J. Am. Chem. Soc.* **131**, 9405-9412, doi:10.1021/ja9039136 (2009).

39 Zhang, Z. *et al.* Three-Dimensionally Oriented Aggregation of a Few Hundred Nanoparticles into Monocrystalline Architectures. *Adv. Mater.* **17**, 42-47, doi:10.1002/adma.200400401 (2005).

40 Ye, J. *et al.* Nanoporous anatase TiO2 mesocrystals: additive-free synthesis, remarkable crystalline-phase stability, and improved lithium insertion behavior. *J. Am. Chem. Soc.* **133**, 933-940, doi:10.1021/ja108205q (2011).

41 Laramy, C. R. *et al.* Understanding nanoparticle-mediated nucleation pathways of anisotropic nanoparticles. *Chem. Phys. Lett.* **683**, 389-392, doi:10.1016/j.cplett.2017.01.050 (2017).

42 Chen, X., Noh, K. W., Wen, J. G. & Dillon, S. J. In situ electrochemical wet cell transmission electron microscopy characterization of solid–liquid interactions between Ni and aqueous NiCl2. *Acta Mater.* **60**, 192-198, doi:10.1016/j.actamat.2011.09.047 (2012).

43 Egglseder, M. S. *et al.* Tiny particles building huge ore deposits – Particle-based crystallisation in banded iron formation-hosted iron ore deposits (Hamersley Province, Australia). *Ore Geol. Rev.* **104**, 160-174, doi:10.1016/j.oregeorev.2018.10.001 (2019).

44 Lin, X., Heaney, P. & E. Post, J. Iridescence in Metamorphic "Rainbow" Hematite. *Gems Gemology* **54**, doi:10.5741/GEMS.54.1.28 (2018).

45 Anand, R. R. & Gilkes, R. J. Variations in the properties of iron oxides within individual specimens of lateritic duricrust. *Soil Res.* **25**, 287-302 (1987).

46 Grotzinger, J. P. & Knoll, A. H. Stromatolites in Precambrian carbonates: evolutionary mileposts or environmental dipsticks? *Annu. Rev. Earth Planet. Sci.* **27**, 313-358, doi:10.1146/annurev.earth.27.1.313 (1999).

47 Zhou, L. & O'Brien, P. Mesocrystals: a new class of solid materials. *Small* **4**, 1566-1574, doi:10.1002/smll.200800520 (2008).